



# The Feasibility of Detecting Supercooled Liquid With a Forward-Looking Radiometer

Ian Stuart Adams , *Member, IEEE*, and Justin Bobak , *Member, IEEE*

**Abstract**—Icing due to supercooled liquid poses a threat to manned and unmanned aircraft. Particularly with the proliferation of unmanned systems, lightweight passive sensors could allow the remote detection of supercooled liquid. A three-dimensional radiative transfer model is utilized to determine the feasibility of a forward-viewing passive sensor for remotely detecting hazardous icing conditions. An analysis of simulated passive microwave spectra for a forward-viewing passive sensor finds dependencies on the liquid water content, cloud distance, and temperature, and sensitivity is noted across the millimeter-wave spectrum. Spectral flattening in the shoulders of molecular resonances corresponds to the presence of clouds, while saturated brightness temperatures near the transition lines are linked to the ambient temperature. A principal component analysis shows significant information content at *G*-band near the water vapor molecular transition, suggesting compact radiometer systems to detect and range supercooled liquid are feasible. Additional information content may be available at *K<sub>a</sub>*-band, suggesting such observations would be useful when size and mass are not constrained.

**Index Terms**—Clouds, millimeter-wave radiometry.

## I. INTRODUCTION

**S**UPERCOOLED liquid water exists in the atmosphere as cloud droplets down to temperatures of  $-40^\circ$  and is an important component of the global radiation budget [1]. These droplets present in mixed-phase clouds pose a hazard to aviation through airframe icing. From 1999 to 2007, there were 62 in-flight icing reports, with approximately half of the incidents resulting in fatalities [2]. Early research efforts into nose- or pod-mounted sensors produced promising results; however, no such systems have been operationally integrated into aircraft. The advent of remotely piloted and autonomous aircraft has renewed interest in developing remote sensors for detecting supercooled liquid, due to the lack of human environmental awareness in unmanned aerial systems. Moreover, the expanded use of *G*-band radiometry, both due to the reduced component size and proximity to the 183.1-GHz water vapor line [3], suggests that a small system for detecting, and even coarsely ranging, supercooled liquid clouds may be possible. Such systems with limited size,

weight, and power consumption would be ideal for unmanned aerial systems.

Simulating the response to horizontally finite clouds adds additional complexity to radiative transfer calculations. To address the icing detector issue, the Air Force Geophysics Laboratory's RADTRAN radiative transfer model was modified to have a concentric-layered atmosphere [4]. While the model was not capable of including scattering ice species for horizontal views, it showed an appreciable response to liquid water droplets at 37 GHz. Simulations at 89 GHz showed a far more muted response to horizontal views, and other frequencies were not considered, nor were finite antenna patterns.

In this paper, we use the atmospheric radiative transfer simulator (ARTS) [5] to simulate the response to a horizontally finite mixed-phase cloud. The three-dimensional (3-D) capabilities ARTS allow for horizontally finite clouds and finite antenna beams. Monte Carlo integration is used to solve the radiative transfer equation in 3-D in a scattering environment. A simple cloud model is created, based on observations of Arctic mixed-phase clouds, to demonstrate the spectral response to variations in liquid water content (LWC) and temperature, and the line-of-sight distance to the cloud is also considered. The Arctic case was chosen due to the significance of supercooled liquid to the modulation of sea ice, as well as the anticipation of increased Naval operations in the Arctic as sea ice recedes in a warming climate. The ability for both environmental observing and military unmanned systems to avoid hazardous icing conditions is desirable for both civilian and defense agencies. Simulations demonstrate the feasibility of a *G*-band sensor for detecting supercooled liquid clouds, with notable dependence on the amount of liquid water as well as the range to the observed cloud. Additional sensitivity to the local ambient temperature is noted. Section II provides an overview of the cloud scenario used in the simulation and the simulation tools. Section III provides the results of the simulations, whereas the discussion and concluding remarks are presented in Section IV.

## II. MODELING OVERVIEW

### A. Atmospheric Scenario

To determine the passive microwave response to clouds at horizontal viewing angles, we constructed a simplified cloud model based on observations of mixed-phase clouds [6]. The profile of liquid, pristine ice, and aggregated snow is shown in Fig. 1. A gamma distribution is used to represent all hydrometeor

Manuscript received September 29, 2017; revised April 23, 2018; accepted May 21, 2018. This work was supported by the Department of the Navy, Office of Naval Research. (Corresponding author: Ian Stuart Adams.)

I. S. Adams was with the Remote Sensing Division, Naval Research Laboratory, Washington, DC 20375 USA. He is now with Mesoscale Atmospheric Processes Laboratory, NASA Goddard Space Flight Center, Greenbelt, MD 20771 USA (e-mail: ian.s.adams@nasa.gov).

J. Bobak is with the Remote Sensing Division, U.S. Naval Research Laboratory, Washington, DC 20375 USA (e-mail: justin.bobak@nrl.navy.mil).

Digital Object Identifier 10.1109/JSTARS.2018.2844684

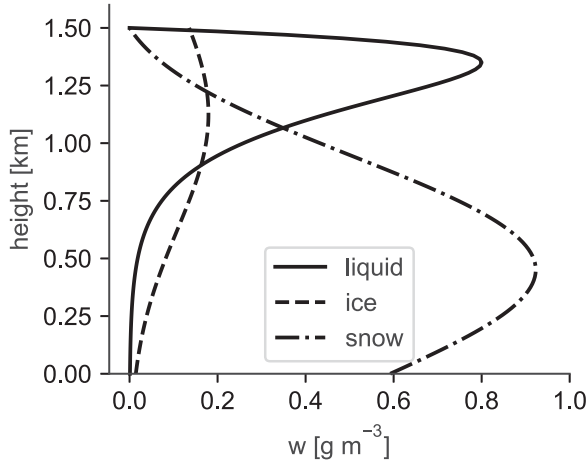


Fig. 1. Cloud profile showing liquid water and two frozen hydrometeor species.

species

$$n(r) = 0 \frac{3 \times 10^{18} w}{4\pi\rho\beta^4\Gamma(\gamma+3)} \left(\frac{r}{\beta}\right)^{\gamma-1} e^{-\frac{r}{\beta}} \quad (1)$$

where  $r$  is the particle radius in  $\mu\text{m}$ ,  $w$  is the water content in  $\text{g}\cdot\text{m}^{-3}$ ,  $\rho$  is the density of liquid or ice water in  $\text{g}\cdot\text{m}^{-3}$ ,  $\gamma$  is a dimensionless shape parameter, and  $\beta = r_e / (\gamma + 2)$ . The effective radius  $r_e$  is the ratio of the third moment of the size distribution to the second. Finally, the number density at each radius  $n(r)$  has units of  $\mu\text{m} \cdot \text{m}^{-3}$ . In this form, changes to water content simply scale the size distribution. The prescribed values of  $r_e$  used in this study for liquid cloud, pristine ice, and aggregated snow are  $10 \mu\text{m}$ ,  $20 \mu\text{m}$ , and  $100 \mu\text{m}$ , respectively, and for the shape parameter, we use  $\gamma = 3$ . The pristine ice crystals are assumed to have planar geometries, based on the growth regime consistent with the temperature within and directly below the liquid layer [7]. For analyzing the response to variation in liquid water, the liquid water profiles are scaled such that the profile peak has values of 0.1, 0.2, 0.4, and  $0.8 \text{ g}\cdot\text{m}^{-3}$ .

The temperature, pressure, diatomic oxygen ( $\text{O}_2$ ), diatomic nitrogen ( $\text{N}_2$ ), water vapor ( $\text{H}_2\text{O}$ ), and ozone ( $\text{O}_3$ ) profiles are taken from the Air Force Geophysics Laboratory Atmospheric Constituent Profiles [8] database included with the ARTS supplementary data, specifically the zonal-mean profiles for subarctic winter. The temperature and derived relative humidity profiles, which are germane to the results presented in Section III, are shown in Fig. 2. The water vapor profile has been converted from volume mixing ratio to relative humidity

$$\text{RH} = \text{VMR} \frac{p}{e_s} \times 100\% \quad (2)$$

where  $p$  is the pressure and  $e_s$  is the saturation vapor pressure [9] over water, both in pascal. The relative humidities at the bottom of the column of the table are adjusted so that the layers in which clouds are present are near saturation with respect to liquid. For input into the radiative transfer model, the humidity profile is then converted back into the volume mixing ratio based on the shifted temperature profile, where the entire temperature profile

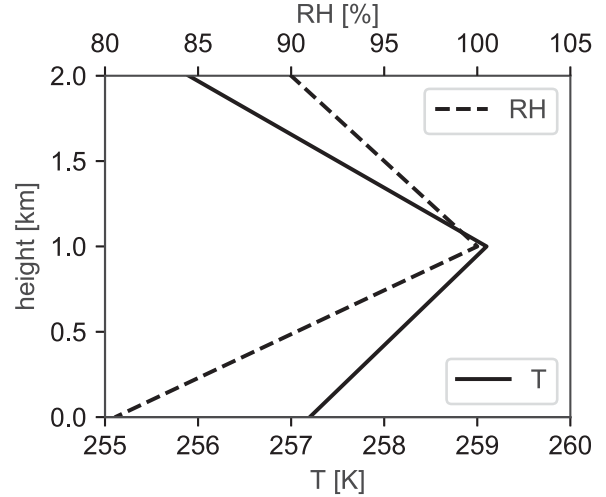


Fig. 2. AFGL subarctic winter temperature profile [8] and modified humidity profile.

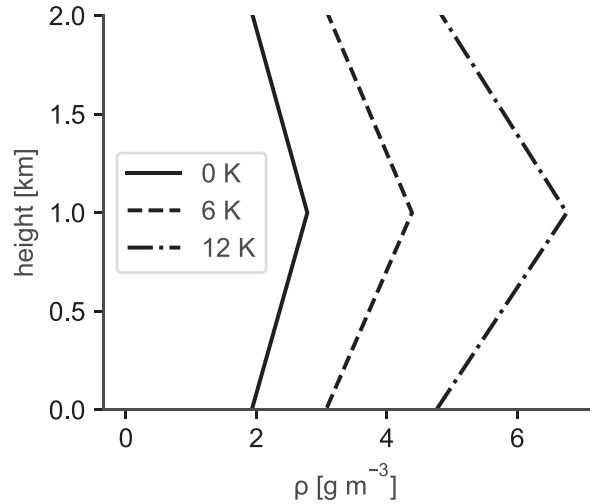


Fig. 3. Profiles of water vapor mass density, based on the relative humidity profile, for the prescribed temperature shifts of 0, 6, and 12 K. The corresponding columnar-integrated water vapor values are 9.5, 15.2, and 23.9 mm, respectively.

is shifted by 0, 6, and 12 K, which results in columnar water vapor amounts of 9.5, 15.2, and 23.9 mm, respectively. The resulting water vapor mass density profiles within the region of interest are shown in Fig. 3. When the temperature profile is shifted, the pressure profile is adjusted such that the ratio of pressure to temperature remains constant.

The model atmosphere varies vertically, but is horizontally homogeneous. The one exception is that since the 3-D nature of the radiative transfer model allows for horizontally finite clouds, the cloud extends 111.3 km (or  $1^\circ$  equatorial longitude on a spherical Earth model) along the sensor flight direction and 556.6 km perpendicular to the flight direction. The spatial dimensions of the cloud are consistent with observed Arctic clouds: shallow in vertical extent, but extended horizontally. Such clouds persist, on average, for 12 h, but can have lifetimes of many days [10].

### B. Radiative Transfer Description

To perform radiative transfer simulations, we used the ARTS version 2.3 [5]. The ARTS is a publicly available open-source suite of tools for performing radiative transfer in spheroidal planetary atmospheres, including Earth, where geometries can range from one to three dimensions. A number of gaseous absorption models are available for internally calculating atmospheric absorption, and a collection of scattering solvers are included for including hydrometeors at frequencies where scattering must be considered. The framework is controlled using a native scripting language that allows users to choose relevant modules based on the radiative transfer problem. These features make the ARTS well suited for solving the radiative transfer equation for a horizontal-viewing radiometer.

For the purposes of simulating radiances in a 3-D atmosphere with scattering species, we utilize reverse Monte Carlo integration, which can also account for multiple scattering effects [11]. To handle the nondiagonal extinction matrices inherent with horizontally aligned particles, the reverse Monte Carlo algorithm relies on importance sampling, a technique that allows independent variables to be drawn from an arbitrary distribution, contingent upon the final integral being appropriately weighted. More specifically, for the present case, the first Stokes parameter is considered the most important when randomly calculating reverse propagation path lengths based on the extinction matrix, which is a good assumption considering that the first and second Stokes components typically differ by one-to-two orders of magnitude for passive millimeter-wave remote sensing applications. Uniformly distributed random numbers are drawn to determine both propagation path length and scattering direction. Gaussian-distributed random numbers are used to determine the line-of-sight azimuth and zenith directions at the sensor, and azimuth and zenith half-power beamwidths are specified to emulate quasi-realistic antenna patterns. Monte Carlo standard error is germane to the simulation setup, which is a measure of convergence

$$e(I) = \sqrt{\frac{\langle I^2 \rangle - \langle I \rangle^2}{N}} \quad (3)$$

where  $I$  is the first Stokes parameter and  $N$  is the number of integrated photons. Furthermore, details on the reverse Monte Carlo solver are available in [11].

This model has been used to simulate brightness temperatures for space-based sensors for both limb [12] and conical [13] geometries, producing synthetic radiances that are consistent with observations. It has also compared well with other models for ground-based geometries [14]. While the simulation horizontal of geometries is relatively novel, the performance of the model for other geometries gives us confidence for using the ARTS and the reverse Monte Carlo solver in this study.

Hydrometeor scattering properties for ice particles are calculated using the T-Matrix method for fixed orientation [15] with a temperature-dependent complex permittivity for ice [16]. Pristine ice particles are represented with cylindrical plates of solid ice with a 4:1 aspect ratio, and aggregates are oblate spheroids with an aspect ratio of 1.33:1 and a density of  $0.2 \text{ g}\cdot\text{cm}^{-3}$ . The

effective permittivity is calculated using the Maxwell–Garnett mixing formula for elliptical inclusions [17], with a lattice of ice containing inclusions of air. While T-Matrix calculations are not as representative as the higher fidelity discrete dipole approximation [18] for frozen hydrometeors with irregular shape, a comprehensive database of digital differential analyzer computed particles is not available for preferentially aligned snow particles with random azimuthal orientation. Moreover, pristine particles of small sizes, such as those at the location of the liquid layer, can be modeled well using idealized but representative geometries [19].

The von Mises distribution [20], which is a good directional statistics approximation of a Gaussian distribution, is used to characterize particle flutter. Defined over a semicircle

$$p(\theta) = \frac{e^{\kappa \cos(2(\theta-\mu))}}{\pi I_0(\kappa)}. \quad (4)$$

The parameters  $\mu$  and  $\kappa$  give the mean and spread of the distribution, with  $\kappa$  being inversely proportional to standard deviation. For the frozen hydrometeors, flutter is defined with a spread parameter of seven (Gaussian-equivalent standard deviation of approximately  $11^\circ$ ).

Supercooled cloud liquid droplets are modeled as a spherical scattering species using the T-Matrix for random orientations [21] with complex permittivity prescribed by Turner *et al.* [22]. Gas absorption for  $\text{N}_2$ ,  $\text{O}_2$ , and  $\text{H}_2\text{O}$  is calculated using the complete Rosenkranz absorption model [23]–[25], with improvements to  $\text{O}_2$  absorption [26]. Absorption for  $\text{O}_3$  is calculated using line data from the HITRAN catalog [27]. While the contribution of  $\text{O}_3$  is expected to be minimal, as the volume mixing ratios in the troposphere are two orders of magnitude below the upper atmosphere peak, ozone is included for completeness, and the inclusion of  $\text{O}_3$  requires negligible computing resources.

### III. SIMULATION RESULTS

In the simulations, the sensor is placed at an altitude of 1.35 km, which corresponds to the peak in the LWC, and we prescribe a half-power beamwidth of  $1^\circ$  at all frequencies (30 to 200 GHz). The choice of a  $1^\circ$  beamwidth allows some impact of beam spreading for more realistic results. While achieving a  $1^\circ$  beamwidth at 30 GHz would require a large ( $>1 \text{ m}$ ) aperture, the point of these simulations is to look at the signature and not immediately be constrained by potential implementations. In the next phase, when frequency choices for a retrieval algorithm are considered, simulations at appropriate beamwidths, which may be tailored to specific frequency choices, will be performed. The spectrum is sampled at 2-GHz intervals. The Monte Carlo standard error is set to 0.2 K; however, there are some points at high optical depth that converge rapidly but get stuck at the saturation temperature. While the Monte Carlo error for the  $I$  component of the Stokes vector for these points is below the standard error threshold, the error in  $Q$  (polarization difference) remains high. Future modifications to the Monte Carlo integration will take the convergence of  $Q$  into account. To remove these anomalous points, spectra are processed with a three-element median

filter, but some artifacts can remain at the edges of spectral line features or when consecutive frequencies are saturated. The ice water content is not varied in this paper, and the peak amount of ice is extreme for Arctic mixed-phase clouds. However, simulations comparing icy and no-ice scenarios differ by no more than 1 K.

#### A. Varying LWC

Placing the sensor 25.6 km from the cloud edge, we look at the dependence on LWC. For this exercise, the profiles are scaled such that the peak LWC has values of 0.1, 0.2, 0.4, and 0.8  $\text{g}\cdot\text{m}^{-3}$ , corresponding to vertically integrated quantities of 0.04, 0.08, 0.16, and 0.33  $\text{kg}\cdot\text{m}^{-2}$ , respectively. The resulting spectra are shown with solid lines in the top panel of Fig. 4, and the clear sky spectrum is given for reference. The response is fairly monotonic with increasing liquid for window regions of the spectra. Near molecular resonances (60 and 118 GHz for  $\text{O}_2$  and 183.31 GHz for  $\text{H}_2\text{O}$ ), the spectra are saturated at a temperature below the local ambient temperature of 258 K. For 60-GHz  $\text{O}_2$  complex, the brightness temperature saturates at 256.6 K for all cloud conditions, including no cloud. At 118 GHz, there is variation of 1 K between 254 (clear sky) and 255 K (saturated), with the brightness temperature quickly saturating with increasing cloud. This is not surprising as this spectral feature is weaker than the 60 GHz oxygen complex. The brightness temperatures are saturated at 253.6 K at the 183.31 GHz water vapor line. Compared with the remote (25.6 km) view of the cloud, the spectra are much more compressed when the sensor is located 7.8 km from the cloud edge (dashed line). There is some difference in compression for the different window regions (30–50 GHz versus 75–110 GHz versus 130–170 GHz). Below 50 GHz, there is still considerable variation in the spectra over the range of an LWC. In the middle-window region, there is still some dependence to LWC, but the spectra eventually saturate at the highest water content values. In the highest window region, the spectra quickly saturate, although there is some variation for lower amounts of liquid water.

Highlighting the spectral response near the  $\text{H}_2\text{O}$  molecular transition at 183.1 GHz, in Fig. 5, we see significant spectral flattening with increasing LWC and decreasing distance to the cloud edge. Looking at the differential brightness temperatures between the line peak (183.1 GHz) and 170 GHz, the clear sky case is about 13.7 K. For 0.8  $\text{g}\cdot\text{m}^{-3}$  at 25.6 km, this compresses to 8.7 K, and for the same amount liquid water, but only 7.8 km from the cloud, it is 0 K.

#### B. Varying Distance

A similar exercise is performed fixing the LWC at 0.1  $\text{g}\cdot\text{m}^{-3}$ , and varying the sensor location. Table I provides the line-of-sight distance between the sensor and the cloud edge along the sensor boresight, along with the vertical displacement from the liquid peak at the cloud pierce point. For the distances given, the line-of-sight distance deviates from the arc distance by less than 10 m at the farthest point. Additionally, diameter of the projected beam at the half-power level is given to show that the increase in vertical displacement with distance is a fraction of

the beam diameter. The boresight of the antenna is shifted less than one-sixth of the half-power beamwidth at the farthest distance, but there is increased smoothing of the brightness temperature contribution from the liquid layer with distance.

As with the liquid water dependence, the sensor response to changing distance is monotonic in window regions and saturated at the molecular resonances, as shown in the center panel of Fig. 4 (solid lines), with the saturation temperatures matching those from the simulations of varying liquid. Above the 60-GHz  $\text{O}_2$  lines, the spectral flattening with decreasing distance is similar to the spectral flattening with increasing water content; however, at lower frequencies (below 50 GHz), the spectral flattening is not quite as strong as the liquid water response. When the liquid water is increased to 0.4  $\text{g}\cdot\text{m}^{-3}$  (dashed lines), there is additional flattening of the spectra, and the middle and upper window regions become saturated.

#### C. Shifting Temperature Profile

The third parameter for which we investigate  $T_b$  response is temperature, looking at clear sky simulations (solid) and simulations where the LWC was set to 0.4  $\text{g}\cdot\text{m}^{-3}$  (dashed). The sensor is located 16.7 km from the cloud edge. These simulation results are shown in the bottom panel of Fig. 4. Near the molecular transitions where the spectra saturate, the shifts in the temperature profiles result in equal shifts of the spectra. For the window regions, the behavior is much more complex due to the commensurate changes in water vapor. By holding the relative humidity constant while the temperature is increased, the  $\text{H}_2\text{O}$  volume mixing ratio is increased by a factor of 2.5 to 2.6 in the region of interest for a 12-K temperature shift.

#### D. Dimensionality Reduction

Principal component analysis (PCA) is typically applied to reduce the dimensionality of high-dimensional systems. While the free parameters that we investigate comprise an artificially low-dimensional system, additional parameters (namely, pressure and  $\text{H}_2\text{O}$ ) change with shifts to the temperature profile. Hence, we use PCA to elucidate the information content of the performed simulations. In performing this analysis, we are ignoring the inherent nonlinearities and non-Gaussian behavior of the simulated system. The variations in liquid water, distance, and temperature are those listed previously.

Fig. 6 shows a scatter plot of the first two principal components, with the colormap corresponding to frequency. There is an obvious separation in behavior between the low frequencies (below 50 GHz) and the high frequencies. Frequencies near the molecular transitions have low scores in the first principal component, which reflects the saturation with respect to LWC and distance. The *W*-band window region spans a similar, albeit wider, range of scores in the first principal component, compared with the *G*-band window region, suggesting both some level of redundancy along with slightly increased sensitivity at *W*-band.

The three window regions are stratified with respect to the second principal component, with the window region between 70 and 110 GHz having the lowest scores. Notably, both the



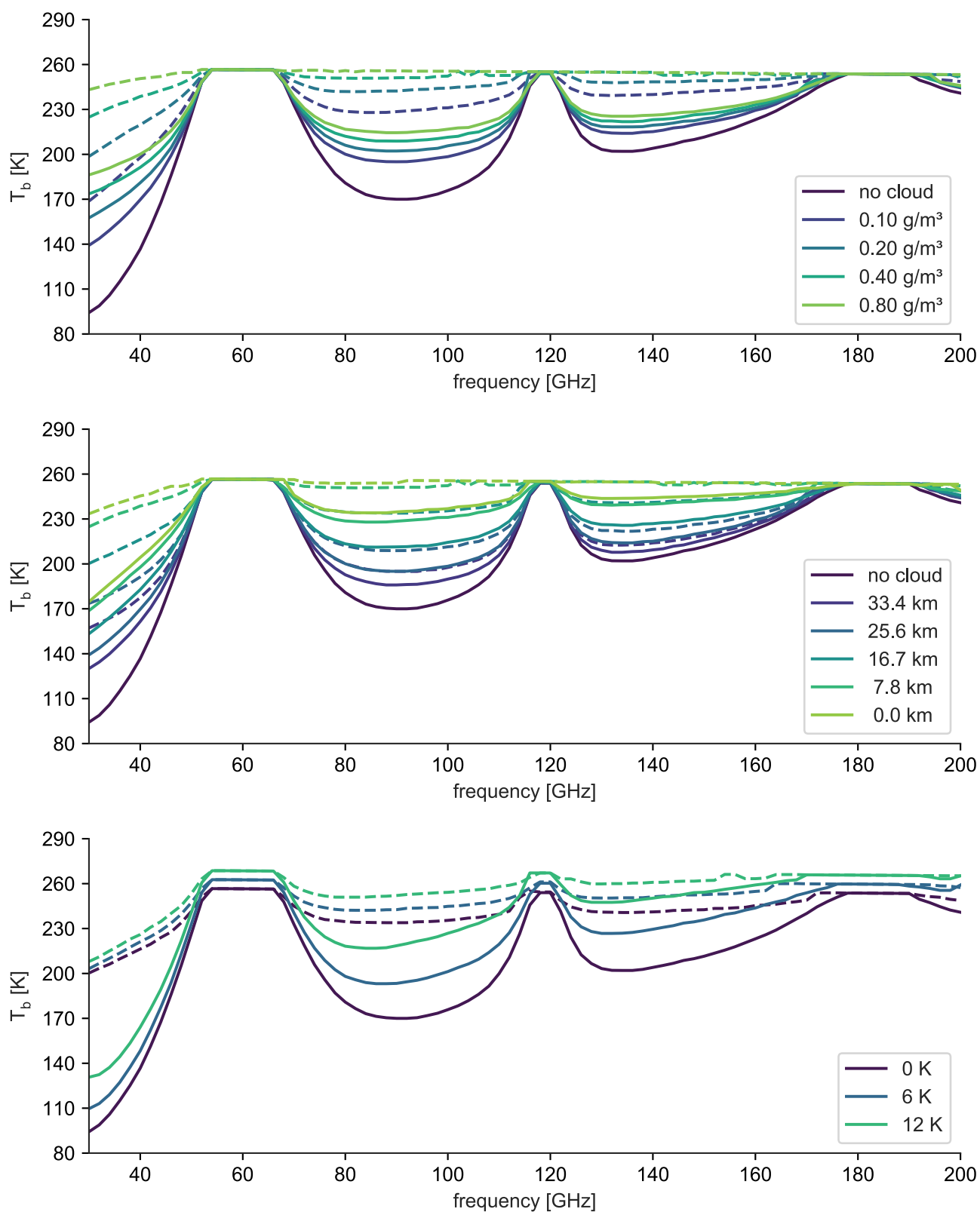


Fig. 4. Passive microwave  $T_b$  spectral dependence on LWC (top), range to cloud (middle), and temperature (bottom). When testing the dependence on LWC, the distance from the cloud edge was set to 25.6 km (solid) and 7.8 km (dashed). To demonstrate the dependence on cloud range, the LWC was fixed at  $0.1 \text{ g}\cdot\text{m}^{-3}$  (solid) and  $0.4 \text{ g}\cdot\text{m}^{-3}$  (dashed). When adding temperature shifts to the database temperature profile, the sensor was placed 16.7 km from the cloud edge for clear sky (solid) and LWC of  $0.4 \text{ g}\cdot\text{m}^{-3}$  (dashed). For reference, the clear sky spectrum is also shown in the top and middle panels.

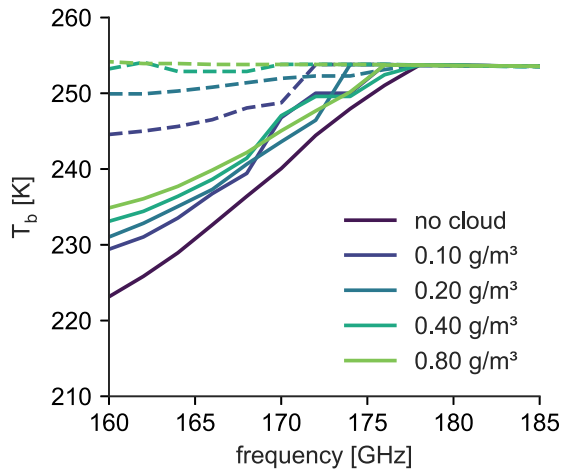


Fig. 5. Same as the top panel of Fig. 4, but with the axes limited to highlight the spectral response at  $G$ -band near the 183.1  $H_2O$  absorption line.

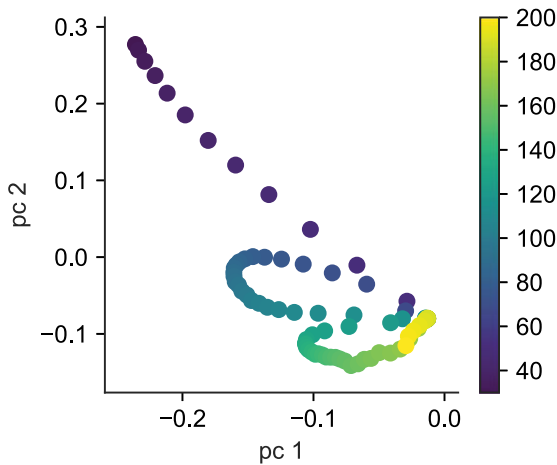


Fig. 6. First two principal components, colormapped to frequency.

TABLE I  
SENSOR GEOMETRY

Distance (km)	Displacement (m)	Diameter (m)
0.00	0.00	0.00
7.79	4.76	136
16.7	21.8	292
25.6	51.4	447
33.4	87.4	583

portions of the  $G$ -band spectrum near the  $H_2O$  line, as well as  $K_a$ -band frequencies, exhibit appreciable scores in both principal components, while also populating very different regimes in principal component space, suggesting that these two regions of the millimeter-wave spectrum contain unique and complementary information.

#### IV. CONCLUSION

The simulations demonstrate that liquid cloud layers can be detected using a forward looking radiometer, and that the spectral response to the cloud depends both on distance and LWC.

One challenge going forward will be choosing and channel set and developing inversion methods to separate the response to LWC and distance. Given that the liquid water response saturates near molecular resonances for fixed distance and distance response saturates for fixed water content, and the saturation brightness temperature shifts with the temperature of the atmosphere, rough determination of ambient temperature is also possible, especially if the local atmospheric transmission coefficient is known or can be estimated. The results suggest significantly larger responses than previous studies at 37 and 89 GHz [4]; however, the noncloud atmospheric conditions used in this study may differ considerably from the previous work due to our choice of the Arctic domain.

The spectral flattening in the window region near the 183.31-GHz water vapor transition due to liquid clouds has been observed in preliminary experiments with horizontal-viewing  $G$ -band radiometers (Randolph Ware, private communications). While this suggests that the phenomenology is sound, additional simulations and observations of matching conditions are necessary for a full quantitative comparison between modeling and measurements. Future efforts look to incorporate cloud resolving model or observed cloud and precipitation data into the radiative transfer framework, as we have done in previous studies [13], [28], to investigate more representative atmospheric scenarios for forward-viewing sensors. Midlatitude systems that contain larger ice particles and snow aggregates with embedded liquid layers will be included to determine the effects of larger scatterers, as the impact of ice on the present simulations is minimal. Future simulations will also make use of refractive bending capabilities in ARTS.

Given the simulated responses, millimeter-wave, in particular  $G$ -band, sensors that will allow for reduced size and mass are feasible systems for detecting liquid clouds. Furthermore, state-of-the-art radiometers in this band have demonstrated sensitivities on the order of 0.1 K [29], which is lower than the Monte Carlo standard error and is more than sufficient for these purposes. However, the PCA suggests that additional information may be gained by including  $K_a$ -band radiometers when size, mass, and power constraints are of less concern.

While the results of this study suggest exploitable radiometric sensitivity to liquid water clouds for horizontal lines of sight and should be used to support sensor development, future studies will be necessary using realistic cloud scenarios over a range of geographical domains to determine optimal channel sets, as well as other sensor characteristics. Additionally, retrievals using the synthetic results will be required to assess the expected performance over a range of conditions. Higher fidelity simulations would then need to be verified with field measurements in similar conditions.

#### REFERENCES

- [1] A. V. Matus and T. S. L'Ecuyer, "The role of cloud phase in Earth's radiation budget," *J. Geophys. Res. Atmos.*, vol. 122, no. 5, pp. 1196–2578, 2017.
- [2] A. Reehorst *et al.*, "Progress towards the remote sensing of aircraft icing hazards," Nat. Aeronaut. Space Admin., Washington, DC, USA, Tech. Rep. NASA/TM-2009-215828, Nov. 2009.

- [3] W. J. Blackwell, "Radiometer development for small satellite microwave atmospheric remote sensing," in *Proc. IEEE Int. Geosci. Remote Sens. Symp.*, Jul. 2017, pp. 267–270.
- [4] G. G. Koenig, C. C. Ryerson, and J. A. Nagle, "Using RADTRAN to simulate an aircraft microwave radiometer to detect icing potential," in *Proc. 42nd Aerosp. Sci. Meeting Exhib.*, 2004, pp. 141–144.
- [5] S. A. Buehler, J. Mendrok, P. Eriksson, A. Perrin, R. Larsson, and O. Lemke, "ARTS, the atmospheric radiative transfer simulator – version 2.2, the planetary toolbox edition," *Geosci. Model Develop.*, vol. 11, no. 4, pp. 1537–1556, 2018.
- [6] M. D. Shupe *et al.*, "A focus on mixed-phase clouds," *Bull. Amer. Meteorol. Soc.*, vol. 89, pp. 1549–1562, Oct. 2008.
- [7] K. G. Libbrecht, "The physics of snow crystals," *Rep. Progress Phys.*, vol. 68, no. 4, pp. 855–895, 2005.
- [8] G. P. Anderson, S. A. Clough, F. X. Kneizys, J. H. Chetwind, and E. P. Shettle, "AFGL atmospheric constituent profiles," Air Force Geophys. Lab., Air Force Base, OH, USA, Tech. Rep. AFGL-TR-86-0110, May 1986.
- [9] A. Wexler, R. Hyland, and R. Stewart, *Thermodynamic Properties of Dry Air, Moist Air and Water and SI Psychrometric Charts*. Atlanta, GA, USA: ASHRAE, 1983.
- [10] M. D. Shupe, S. Y. Matrosov, and T. Uttal, "Arctic mixed-phase cloud properties derived from surface-based sensors at SHEBA," *J. Atmos. Sci.*, vol. 63, no. 2, pp. 697–711, 2006.
- [11] C. Davis, C. Emde, and R. Harwood, "A 3D polarized reverse Monte Carlo radiative transfer model for mm and sub-mm passive remote sensing in cloudy atmospheres," *IEEE Trans. Geosci. Remote Sens.*, vol. 43, no. 5, pp. 1096–1101, May 2005.
- [12] D. L. Wu, J. H. Jiang, and C. P. Davis, "Eos mls cloud ice measurements and cloudy-sky radiative transfer model," *IEEE Trans. Geosci. Remote Sens.*, vol. 44, no. 5, pp. 1156–1165, May 2006.
- [13] I. S. Adams and M. H. Bettenhausen, "Brightness temperature simulation of observed precipitation using a three-dimensional radiative transfer model," *J. Atmos. Ocean. Technol.*, vol. 33, no. 10, pp. 2053–2064, 2016.
- [14] A. Battaglia, C. P. Davis, C. Emde, and C. Simmer, "Microwave radiative transfer intercomparison study for 3-d dichroic media," *J. Quant. Spectrosc. Radiative Transfer*, vol. 105, no. 1, pp. 55–67, 2007.
- [15] M. I. Mishchenko, "Calculation of the amplitude matrix for a nonspherical particle in fixed orientation," *Appl. Opt.*, vol. 39, pp. 1026–1031, Feb. 2000.
- [16] C. Mätzler, "Dielectric properties of natural media: Microwave dielectric properties of ice," in *Thermal Microwave Radiation: Applications for Remote Sensing*, C. Mätzler, Ed. Stevenage, U.K.: Inst. Eng. Technol., 2006, pp. 455–463.
- [17] S. Giordano, "Effective medium theory for dispersions of dielectric ellipsoids," *J. Electrostat.*, vol. 58, no. 1, pp. 59–76, 2003.
- [18] B. T. Draine and P. J. Flatau, "Discrete-dipole approximation for scattering calculations," *J. Opt. Soc. Amer. A*, vol. 11, no. 4, pp. 1491–1499, Apr. 1994.
- [19] I. S. Adams and M. H. Bettenhausen, "The scattering properties of horizontally aligned snow crystals and crystal approximations at millimeter wavelengths," *Radio Sci.*, vol. 47, no. 5, 2012, Art. no. RS5007.
- [20] K. V. Mardia, *Statistics of Directional Data*. London, U.K.: Academic, 1972.
- [21] M. I. Mishchenko and L. D. Travis, "Capabilities and limitations of a current FORTRAN implementation of the T-matrix method for randomly oriented, rotationally symmetric scatterers," *J. Quant. Spectrosc. Radiative Trans.*, vol. 60, pp. 309–324, Sep. 1998.
- [22] D. D. Turner, S. Kneifel, and M. P. Cadetdu, "An improved liquid water absorption model at microwave frequencies for supercooled liquid water clouds," *Amer. Meteorol. Soc.*, vol. 33, pp. 33–44, Jan. 2016.
- [23] P. W. Rosenkranz, "Absorption of microwaves by atmospheric gasses," in *Atmospheric Remote Sensing by Microwave Radiometry*, M. A. Janssen, Ed. New York, NY, USA: Wiley, 1993, pp. 37–90.
- [24] P. W. Rosenkranz, "Water vapor microwave continuum absorption: A comparison of measurements and models," *Radio Sci.*, vol. 33, pp. 919–928, Apr. 1998.
- [25] P. W. Rosenkranz, "Correction to 'water vapor microwave continuum absorption: A comparison of measurements and models'," *Radio Sci.*, vol. 34, p. 1025, Apr. 1999.
- [26] M. Yu. Tretyakov, M. A. Koshelev, V. V. Dorovskikh, D. S. Makarov, and P. W. Rosenkranz, "60-GHz oxygen band: Precise broadening and central frequencies of fine-structure lines, absolute absorption profile at atmospheric pressure, and revision of mixing coefficients," *J. Mol. Spectrosc.*, vol. 231, pp. 1–14, May 2005.
- [27] L. S. Rothman *et al.*, "The HITRAN2012 molecular spectroscopic database," *J. Quant. Spectrosc. Radiat. Transf.*, vol. 130, no. Suppl. C, pp. 4–50, 2013.
- [28] I. S. Adams, P. Gaiser, and W. Linwood Jones, "Simulation of the Stokes vector in inhomogeneous precipitation," *Radio Sci.*, vol. 43, no. 5, 2008, Art. no. RS5006.
- [29] S. T. Brown *et al.*, "The high-altitude MMIC sounding radiometer for the global hawk unmanned aerial vehicle: Instrument description and performance," *IEEE Trans. Geosci. Remote Sens.*, vol. 49, no. 9, pp. 3291–3301, Sep. 2011.

**Ian Stuart Adams** (S'01–M'08) received the Ph.D. degree in electrical engineering from the University of Central Florida, Orlando, FL, USA, in 2007.

From 2004 to 2006, he was a Consultant with Microwave Remote Sensing Consultants, Cocoa Beach, FL, USA. From 2006 to 2017, he was with the Naval Research Laboratory, Washington, DC, USA, where he studied the effects of precipitation on passive polarimetric remote sensing of ocean surface winds as well as vector radiative transfer of clouds and precipitation. He is currently a Research Physical Scientist with the Mesoscale Atmospheric Processes Laboratory, NASA Goddard Space Flight Center, Greenbelt, MD, USA. His research interests include three-dimensional vector radiative transfer in precipitation, active and passive millimeter-wave sensors, and geophysical forward model inversion.

Dr. Adams is a member of the American Geophysical Union and the American Meteorological Society. He was a Vice Chair of the GRSS Frequency Allocation in Remote Sensing Technical Committee from 2010 to 2013.

**Justin Bobak** (M'89) received the Ph.D. degree in electrical engineering from The Pennsylvania State University, University Park, PA, USA, in 1998. His thesis work was on modeling the effects of turbulence on water vapor radiometer measurements.

He was the Principal Investigator for the Airborne Polarimetric Microwave Imaging Radiometer, an instrument designed and built at NRL to underfly SSMIS and WindSat. He worked on reflector coatings, calibration targets, and error budgeting for NRL's MIS effort. He is currently the Electrical Lead for GLO, the GFCR solar Limb Occultation instrument, Newport News, VA, USA. He has more than 20 years of experience in microwave radiometry, including hardware system design, and retrieval algorithm development. He has authored or coauthored 26 publications.

Dr. Bobak is the recipient of two Berman Awards.